6

Nitrogen Enriched Carbon Nanobubbles and Carbon Spheres: A Study Involving Versatile Energy Harvesting, Storage and CO_2 Adsorption Applications

The work described in this chapter has been published in *ACS Applied Nano Materials, 3, 3706-3716.*

Multifunctional carbon nanomaterials have attracted remarkable consideration in various energy conversion and storage devices for their ultrahigh specific surface area, unique morphological features, and excellent electrochemical properties. Here, we report the synthesis of highly ordered mesoporous nitrogen-enriched carbon nanospheres (CS) and nanobubbles (CNB) by a modified Stöber reaction using resorcinol and formaldehyde in the presence of ethylenediamine as the nitrogen source. A comparative study of the prepared CS and CNB nanomaterials have presented here with wide application potential. The counter electrode made of CNB and CS for dye-sensitized solar cells (DSSCs) showed enhanced electrochemical activity for catalytically reducing I^{3-} to I^- and improved capacitive behaviour with less R_{ct} as inferred from Tafel polarization, cyclic voltammetry (CV), electrochemical impedance spectroscopic (EIS) studies. Further, synthesized CS and CNB are used in integration along with highly efficient variations of TiO_2 having different morphology, namely, rod-shaped TiO_2 synthesized at sub-zero temperature and spherical heterostructure TiO_2 with 1% ZnO; showed remarkable photo conversion efficiency (PCE) of 10.40% with improved J_{sc} (20.20 mA/cm^2) and V_{oc} (0.73 V). The enhanced performance of the fabricated DSSC device was owing to the excellent point contact and good conductivity, which offered better charge transportation of electrons with minimum recombination. Additionally, the effect of these materials when used for applications on supercapacitor and as an adsorbent for CO_2 adsorption has been thoroughly examined.

6.1 Experimental techniques

6.1.1 Preparation of Carbon Spheres (CS)

0.6 mL EDA was added to a volume of ethanol and DI H_2O (mixed in 2:5 ratio), which is stirred until complete dissolution. To it was added 0.4 g of resorcinol and 0.6 mL formaldehyde (37 wt%). This system was kept stirring for 24 hours at 30 °C. The content is then transferred to a steel-lined autoclave having a volume of 125 mL kept in an oven at 100 °C for 24 h. After which, it is centrifuged at 10000 rpm at -6 °C for 15 min. The precipitate is collected and dried in air for 12 h. Annealing is done under N_2 atmosphere at 600 °C for 2 h.

6.1.2 Preparation of Carbon Nanobubbles (CNB)

3.2 mL liquor ammonia solution and 3 mL TEOS are added to DI H_2O and ethanol mixed in a ratio of 7:1. To this reaction mixture 0.21 g resorcinol, 0.31 mL formaldehyde (37 wt%), and 0.10 mL EDA were added subsequently. Further same procedure was followed similar to the preparation of CS. Finally, after annealing etching was performed using HF (50 wt%) solution then washed with ethanol followed by drying at 50 °C for 12 h.

6.1.3 Electrode and Device Fabrication

All solar cells (DSSCs) were fabricated by the same procedure as mentioned in our previous study.(Shejale, Laishram et al. 2016) CNB and CS are individually mixed with our previously reported ZnO doped TiO_2 and TiO_2 synthesized at -40 °C in the wt%. However, CNB and CS loading % are varied, like 0.5, 1, 2, and 5%. CNB and CS based counter electrodes are prepared

by screen printing suspension of Nafion : ethanol (1:1) and synthesized carbonaceous nanoparticles and annealed at 450 °C in air for 30 min after overnight drying in air at room temperature. Standard three-electrode set up was used to analyze the electrochemical performance of both materials, Pt mesh as the counter electrode, SCE (Saturated calomel electrode) as a reference electrode and the prepared materials as the working electrode. For working electrode, as-synthesized sample, polyvinylidene difluoride (PVDF), and carbon black at a ratio of 8:1:1 (weight ratio) in the presence of 1-methyl-2-pyrrolidone (NMP) were mixed and pasted on carbon sheet subsequently dried at 100°C for 12 h.

6.2 Results and discussion

6.2.1 Reaction Details

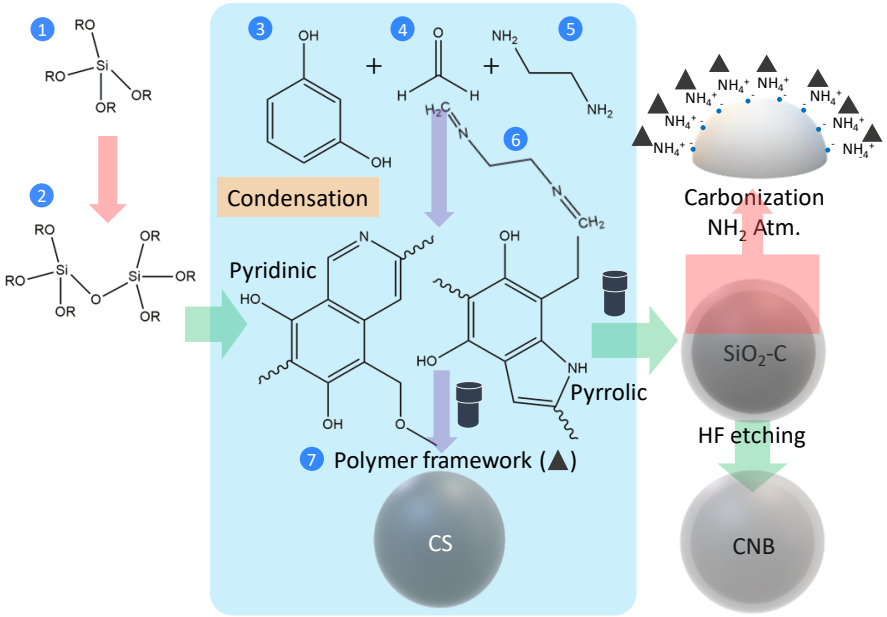

Figure 6.1: Scheme 1. Schematic illustration of the reaction mechanism of CS and CNB formation by modified Stöber reaction. NH_2 Atm. is NH_2 atmosphere, where (1) $Si(OR)_4$, (2) 3D Si-polymer network, (3) Resorcinol, (4) Formaldehyde, (5) Ethylenediamine (EDA), (6) Intermediate compound of (4) and (5) and (7) After excess reaction in between (3) and (4) forms polymer framework

A schematic illustration of the synthesis of CS and CNB by a Stöber reaction is given in Figure 6.1.(Stöber, Fink et al. 1968) The first step in the synthesis of ordered mesoporous carbon nanospheres is the formation of emulsion drops via hydrogen bonding of the various solvents using the precursors EDA, ethanol, water, formaldehyde and resorcinol (1 to 7 from Figure 6.1). Here, EDA is used as a nitrogen source and also as the base catalyst. The ratio of water and ethanol is used to tune the size of the spheres to be formed. The next step of the reaction is the formation of a resin of resorcinol (3) and formaldehyde (4) by polymerization. After which an intermediate of EDA-formaldehyde derived compound (6) gets integrated into the excess resorcinol-formaldehyde network forming the solid polymer spheres. A polymer framework (7) consisting of pyrrolic and pyridinic-type rings are formed by the resorcinol and formaldehyde reaction. The hydrothermal treatment of the formed polymer for 24 h led to formation of uniform colloidal spheres. Finally, a carbonization step of annealing under nitrogen atmosphere results in the formation of carbon spheres (CS). This is a modified Stöber reaction and is illustrated in Figure 6.1. A similar reaction mechanism was adopted for the synthesis of hollow carbon nanobubbles (CNB) whereby TEOS was hydrolysed and condensed (see (1) and (2) compound) to form the core and the RF resin acted as the carbon precursor covering the outer shell. The reaction between the resorcinol and formaldehyde (7) results in intermediates diffusing on the surface, an effect of the presence of NH_4^+. This results in the formation of a polymeric resin sphere.(Liu, Qiao et al. 2011) A stable colloidal suspension of the negatively

charged sphere surrounded by positively charged NH_4^+ is formed, the interaction of which stabilizes and prevents the spheres from agglomerating.(Fuertes, Valle-Vigón et al. 2012) Further after hydrothermal reaction, core SiO_2 is etched by HF treatment with above carbonization step to obtain hollow carbon nanobubbles.

6.2.2. Morphological, Textural and Structural Analysis

The synthesized materials were subjected to morphological analysis using FESEM and TEM to confirm the formation of hollow carbon nanobubbles (CNB) and solid carbon spheres (CS). FESEM images at different magnification can be observed for both CNB and CS in Figure (6.2a, b and c) and (6.2d, e and f) respectively, indicating a highly uniform distribution of the synthesized nanomaterials. The hollow nature of the CNB can be confirmed from the higher magnification images in Figure 6.2b and c whereby the underlying spherical layers can be seen through the transparent spheres of the first layers, unlike for CS in Figure 6.2e and f. This result is furthermore segmented by the TEM results in Figure 6.3a and 6.3b showing hollow CNB against solid CS in Figure 6.3d and e.

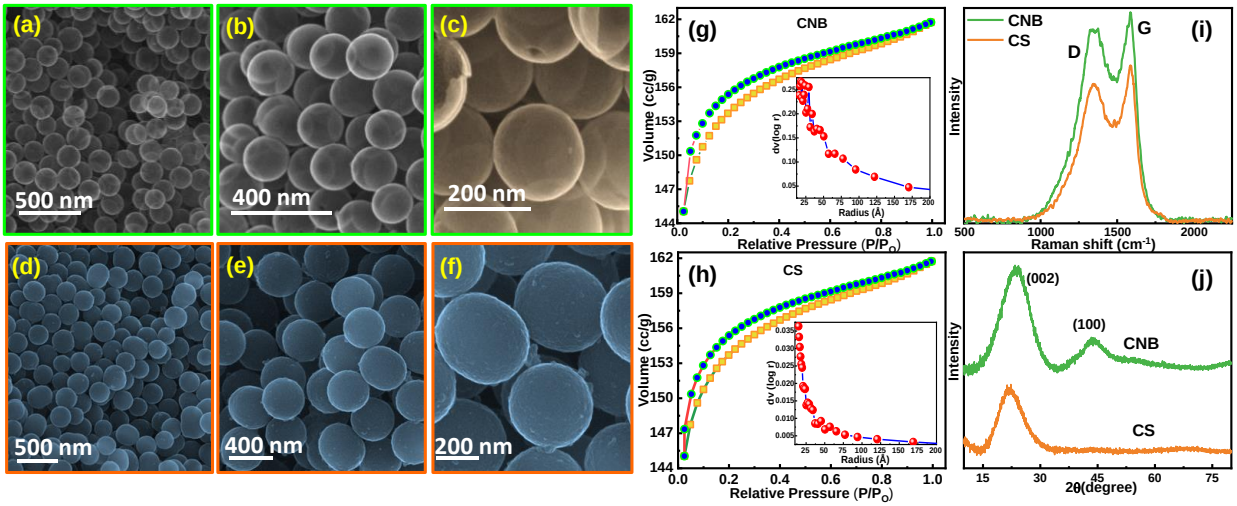

Figure 6.2: FESEM at different magnifications of (a, b and c) CNB and (d, e and f) CS, N_2 adsorption and desorption isotherms of (g) CNB and (h) CS with their respective pore size distribution (inset) in the range of 0.0 to 1.0 relative presses, (i) Raman and (j) XRD spectra (scan rate 0.1°/min).

To realize the change in the pore structure of CS and CNB, N_2 adsorption-desorption BET was performed and the pore size was estimated using the Brauner-Joyner-Halenda (BJH) method (Figure 6.2g and h). Both CS and CNB showed H4 type hysteresis loop with isotherm similar to type I. This indicates that the synthesized materials are of microporous nature. The filling of micropore type observes high uptake at relatively low pressure because of high adsorption potential due to the narrow pore structure as shown in the inset of Figure 6.2g and h. The hysteresis did not show any limiting absorption at high P/P_0 with narrow pores with slits even within the micropores. The hysteresis loop at low pressure is possibly due to swelling of non-rigid pores and uptake of adsorbent molecules with pores similar size to that of the adsorptive molecule.(Lowell, Shields et al. 2004)

Table 6.1. Surface porosity and chemical composition of CNB and CS.

Sample	*N_2 adsorption at (-196 °C) (from N_2 BET)*			*CO_2 adsorption 298 K, (t-plot)*	*Chemical compositions (calculated from EDS)*		
	S_{BET} (m^2g^{-1})	*V_{BET} (cm^3g^{-1})*	*Pore size (nm)*	*S_{micro} (m^2/g^{-1})*	*C (wt%)*	*O (wt%)*	*N (wt%)*
CNB	360	0.25	17	304	98.77	0.55	0.68
CS	468	0.32	11	333	98.45	0.68	0.87

Additionally, the high uptake observed at relatively low pressure in both cases is an indication of the presence of nanopores within the shell.(Xu, Tang et al. 2015) Analysis of the surface area revealed CS to have higher surface area with 468 m^2/g and pore volume of 0.25 cm^3/g while CNB was found to have a reduced surface area at 360 m^2/g with pore volume 0.32 cm^3/g (refer Table 6.1). Additionally, the average pore radius was calculated to be 17 nm for CNB whereas the CS showed a lower pore radius size of around 10 nm. While it is expected for CNB to have greater surface area than the CS due to its ascertained hollow nature it was found to be otherwise so. It can be due to the fact that the average size of CS is much larger than CNB as can be seen from the TEM image in Figure 6.3. Moreover, solid CS with 0.25 cm^3/g pore volume exhibited a porous nature with asurface area capacity of 468 m^2/g. Thus, the higher amount of N_2 adsorption observed in the BET adsorption desorption isotherms for CS can be attributed to the larger size and the porous nature of each individual spheres. Raman spectroscopy is a significant method of characterization for carbon materials. The observed spectra (Figure 6.2i) observed two peaks distinct to D and G band at 1347 cm^{-1} and 1588 cm^{-1}. The presence of D band is assigned to disordered amorphous carbon whereas G band is due to the in-plane vibrations of crystalline graphitic carbon. I_D/I_G for CS is 0.97 and for CNB is 1.18 which depicts the increasing defects on the latter.(Liu, Mei et al. 2018) The XRD peak (Figure 6.2j) for CS showed a broad peak at 21.86° which can be attributed to low crystallinity and amorphous presence of carbon. Whereas for the CNB two peaks were absorbed at 43.77°, 23.72° which corresponds to (100) and (002) planes which can be attributed to more carbonization at CNB.(Liu, Song et al. 2018)

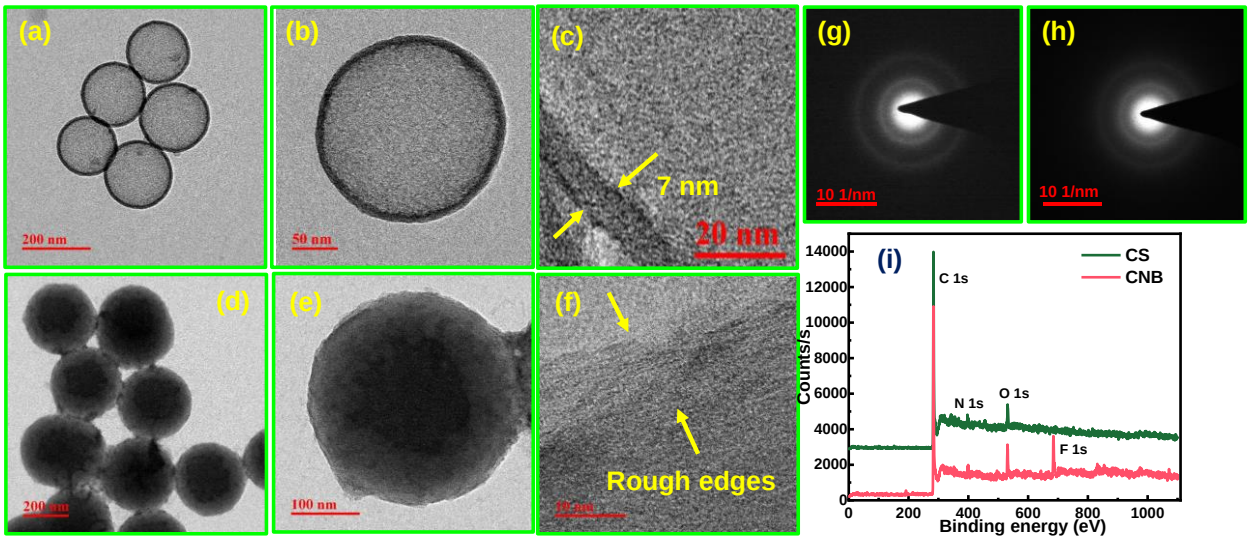

Figure 6.3: TEM images of group, single and HRTEM of CNB (a-c) with mesoporous shell (7 nm) and CS (d-f) with respective SAED pattern (g) and (f). (i) XPS survey spectra of CNB and CS

It can be observed from Figure 6.3b and e that the etching process performed using HF has occurred within the inner part of the silica spheres without affecting the outer shell thickness measuring ~7 nm, as indicated in Figure 6.3c. However, the decrease in the average diameter size in CNB to ~195 nm when compared to ~320 nm of CS might suggest etching of the outer periphery in CNB during the process. Furthermore, there is no defined shell however, rough edges can be seen surrounding the CS can be observed from Figure 6.3f which is also evident by the light grey colour in the outer area surrounding a dark center in Figure 6.3e. Both the Selected Area Electron Diffraction (SAED) pattern in Figure 6.3g and h suggests the amorphous nature of both CS and CNB as depicted in XRD in Figure 6.2j. Further differences are observed in the decomposition of CNB and CS during TG Analysis curves as displayed in Figure 6.4a. The CNB showed decomposition at an initial temperature below 100 °C due to the presence of water vapour and moisture inside the hollow spheres. Furthermore, while both the material completely pyrolyzes at 700 °C, the CS sample showed deferred reaction, which might

be due to the presence of polymer sphere delaying the reaction of organic molecules present in the matrix and the carrier gas, i.e., N_2 gas.

The CNB with hollow core and outer shell were etched by HF solution. The XPS survey scan in Figure 6.3i confirms the presence of C, N and O with the exception of the presence of F in the CNB which might be because of the F^- ion remaining from the HF.

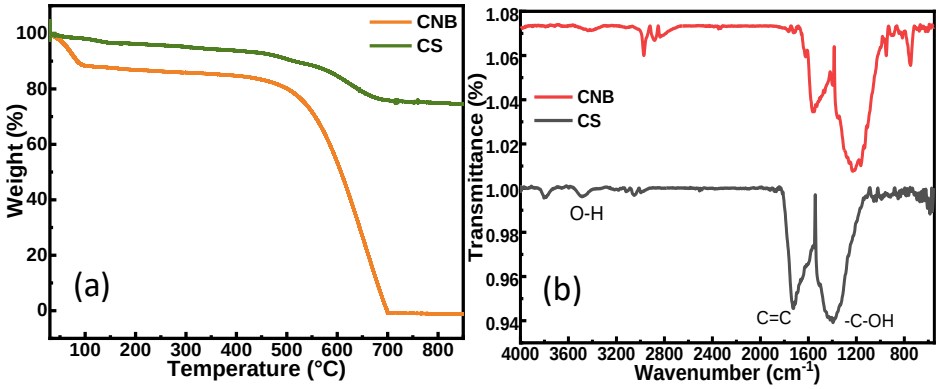

Figure 6.4: TGA curves (a) and FTIR spectra (b) of CNB and CS

Additionally, functional groups present were identified using FTIR measurement (Figure 6.4b) and it can be observed that the IR peaks indicate the presence of similar functional groups. In both the carbon materials, vibrations bands relating to C=O and C=C were observed in bands 1700 cm^{-1} and -C-OH stretching bands were observed at bands around 1300 cm^{-1}. Apart from this, hydroxyl bands were observed for the CNB at around 3500 cm^{-1} which might be the water molecules trapped in the hollow core of CNB. This exhibition of a large number of functional groups stalls the presence of N containing groups thar occurs in a similar region of the IR spectra. For example, C-N stretching occurring at around 1560 cm^{-1} is masked due to the presence of broad aromatic C=C at the region around 1600 cm^{-1}.(Wickramaratne, Xu et al. 2014) A similar overlap was observed for NH_2 vibration with the hydroxyl groups at around 3500 cm^{-1}.(Liu, Xie et al. 2017) Thus, the presence of N containing groups is not well resolved due to the overlap. Additionally, an increase in absorption at the region around 1600 – 1700 cm^{-1} might be due to the increase in the C-N aromatic stretching.

6.2.3. Chemical Analysis

To better understand the chemical states of the synthesized carbon materials, XPS measurements were carried out (Figure 6.3i and 6.5). The high-resolution scan of N 1s XPS peaks was fitted using a Gaussian function to four peaks corresponding to pyridinic N and pyrrolic N at approximately 397 eV and 400 eV for both CNB and CS as shown in Figure 6.5a and 6.5b. The peak occurring at 401 eV can be assigned to quaternary N. In contrast, peaks at higher binding energies can be assigned to oxidize pyridinic N for CS and CNB respectively at 402.5 eV and 404.58 eV. The integrated peak areas for the respective N species are given in Table 1, and it can be observed that there is a change in the peak areas suggesting a change in the N bonding sites during the formation of CS and CNB. The % proportions of the pyridinic N decreases for CNB whereas pyrrolic N, quaternary, and oxidized pyridinic N increases. The quaternary N is reported to increase the conductivity of carbon material whereas pyridinic N increases the pseudo-capacitive effect.

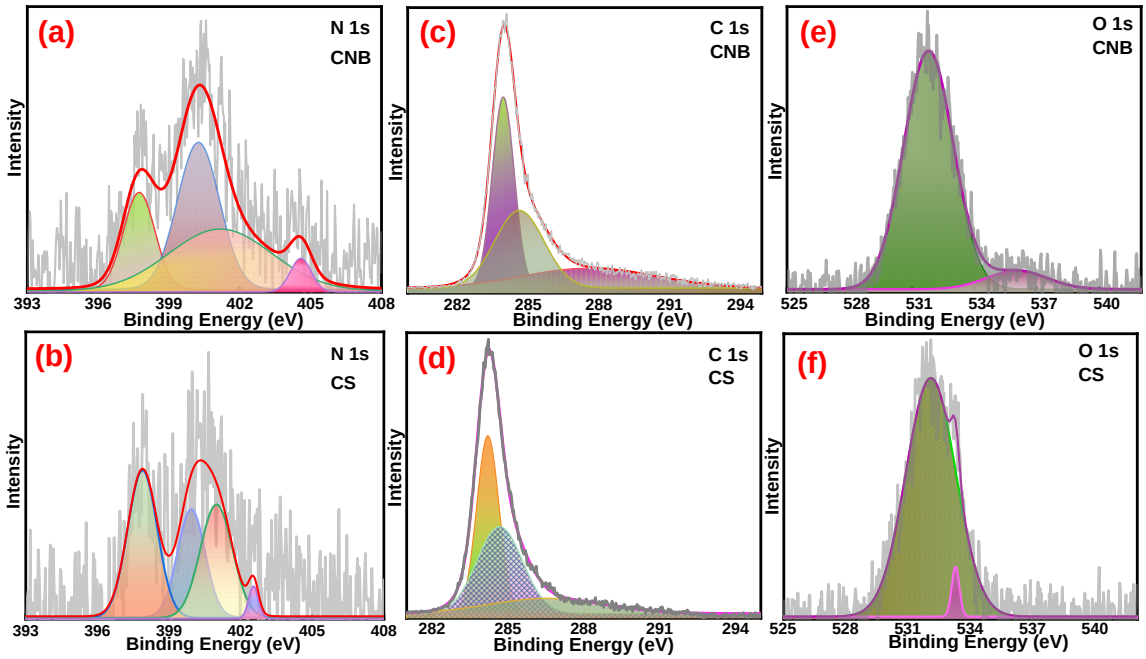

Figure 6.5: High resolution XPS spectra of N 1s (a, b), C 1s (c, d) and O 1s (e, f) spin orbits of the synthesized CNB and CS respectively.

Table 6.2. Distribution of the N components in the synthesized materials

Sample	*Pyridinic N (%)*		*Pyrrolic N (%)*		*Quaternary N (%)*		*Oxidized Pyridinic N (%)*	
	Area (%)	*BE (eV)*	*Area (%)*	*BE (eV)*	*Area (%)*	*BE (eV)*	*Area (%)*	*BE (eV)*
CS	38.58	397.89	26.32	399.93	32.32	400.98	2.78	402.54
CNB	18.70	397.73	37.98	400.24	39.02	401.17	4.30	404.58

Thus, CNB might contribute towards better charge transport.(Xu, Niu et al. 2018) Similarly, in Figure 6.5c and 6.5d, high-resolution C 1s spectra observed three peaks after deconvolution, centred around 284 eV for both CNB and CS that can be assigned to sp^2 hybridized non-oxygenated C i.e., C=C-C. While the peaks at 284.72 eV for CNB and 284.68 eV for CS can be attributed to C-O/C-N. The peak at higher binding energies 286.55 eV and 287.69 eV corresponds to the carboxylate carbon (C=O) respectively for CS and CNB.(Li, Cheng et al. 2016, Xu, Ma et al. 2017) O species present at 531.79 eV and 532 eV correspondingly for CNB and CS can be ascribed to the hydroxyl ions present as shown in Figure 6.5e and 6.5f.(Li, Cheng et al. 2016) The XPS and FTIR establish strongly the presence of nitrogen content in the carbon materials and thus it can be explored for applications relating to CO_2 capture.

6.2.4. Application for CO_2 Capture

Measurements relating CO_2 adsorption were carried out using Quantachrome Autosorb iQ3. The samples were outgassed for 12 h at 200 °C to remove impurities, moisture and other molecules before the start of the adsorption experiment. CO_2 adsorption was performed by measuring the adsorption isotherms of CS and CNB samples and observed parameters are summarized in Table 6.1. As observed from the adsorption isotherm in Figure 6.6a and 6.6b the CO_2 uptake was fast at low pressure and increasing the pressure resulted in increased absorption. There was no apparent saturation level suggesting that there is still capacity to absorb at higher pressure. The mesoporous nature, large surface to volume and nitrogen doping in the synthesized carbon nanomaterials will be viable for use in CO_2 capture applications. The CO_2 adsorption isotherms showing the capacity of adsorption at standard room temperature and pressure for CNB and CS and the number of cycles against the uptake is indicated in Figure 6.6a and b respectively.

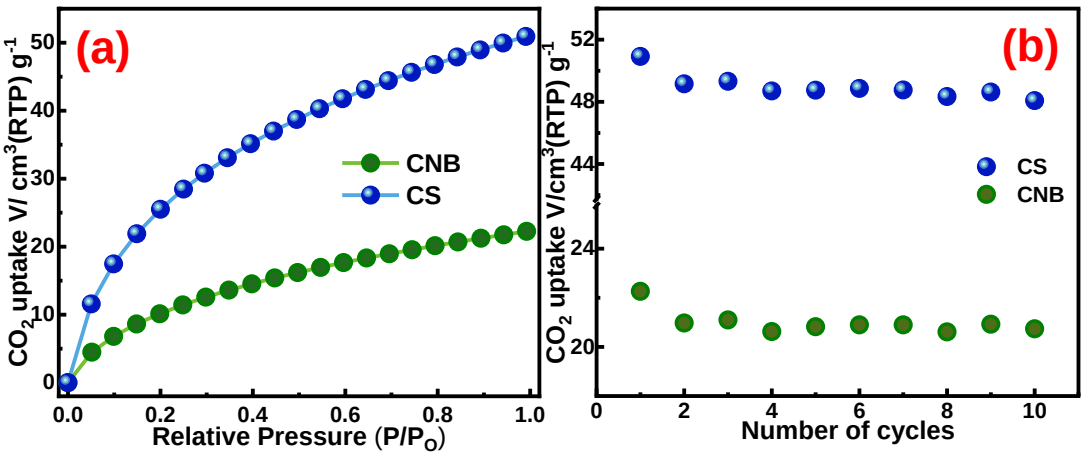

Figure 6.6: CO_2 adsorption (a) and Cycle stability (b) of both the synthesized CS and CNB at 298 K.

On comparison, CS has stronger and steeper adsorption than the CNB counterpart starting from a very low pressure and both carbon nanomaterials did not saturate even at high relative pressure indicating the chances for more adsorption taking place at higher pressure.(Xia, Yu et al. 2016) This shows the strong adsorption between the carbon nanospheres and CO_2 molecules. The adsorption capacity for CS and CNB samples were observed to be around 2 mmol/g and 1 mmol/g respectively. The better adsorption in CS compared to CNB can be attributed to the increased N content that helps to increase the basic nature of the former by changing the surface chemistry, high surface area and as well as an increase in the micropore volume.(Xing, Liu et al. 2012, Li, Guo et al. 2018) Literature reports a strong possibility of carbon atom in the CO_2 molecule to bind strongly with lone pairs of electron existing in N groups in the carbon framework due to its electron-deficient nature.(Liu, Xie et al. 2017) As observed the better CO_2 adsorbing CS based carbon nanomaterial reports higher pyridinic N (from the XPS data in Table 6.2) which is because of the availability of electrons that can be accessed more easily sequentially increasing the basicity in CS based sample.

6.2.5. Application as photoanode for DSSC

Additionally, these synthesized carbon materials are utilized in unison with TiO_2 nanostructures for DSSCs. The synthesis and characterization of these TiO_2 nanostructures were reported earlier by our group.(Shejale, Laishram et al. 2016, Shejale, Laishram et al. 2017) Earlier Kim et al have reported graphitic films embedded onto TiO_2 photoanodes for highly efficient DSSC on the lower, upper and both sides of the photoanode film with the highest recorded efficiency of 5.21 % for the latter. In our study, high performing rice grain morphology TiO_2 synthesized at sub-zero degree temperature (-40 °C TiO_2) and ZnO doped TiO_2 (ZnO-TiO_2) were incorporated along with the synthesized CS and CNB in different combinations to optimize maximum the performance of DSSC device. The photoanodes were prepared by mixing in a mortar pestle with ethylene glycol and α terpineol which was further screen printed on the FTOs (Fluorine doped tin oxide glass, 7-12 Ω/sq). The performance of fabricated DSSCs revealed that the overall efficiency of the device showed great improvement in its performance as given in Table 6.3. A graph showing CS and CNB in varying degree of loading percentages with both ZnO-TiO_2 and –40 °C TiO_2 is given in Figure 6.7a and b with their respective photoconversion efficiency calculated from the DSSC device. To better understand the optimum loading amount for acquiring the highest possible yield, a variation of CNB and CS loading 0.5%, 1%, 2% and 5% was performed for both ZnO doped TiO_2 and TiO_2 synthesized at -40 °C as shown in Figure 6.7d, e, f and g. It can be observed that the 0.5% loading of CNB and CS with both the materials showed the highest efficiency amongst all with high current density of nearly 20 mA/cm^2. It was found that the current density, open circuit potential and the overall efficiency has improved. The evident increase in the V_{OC} and J_{SC} strongly suggests the reduced charge recombination and improvement in the charge collection and transport of charge carrier efficiency in the suggested photoanode composition.(Yu, Fan et al. 2011) Additionally, the increased efficiency can be a cumulative factor of increased surface area leading to better

absorption of dye and efficient trapping of photons. This can be attributed to the spherical morphology increasing the pathway and scattering of light. Thus, the measured current density is highly influenced by the amount of dye absorbed over the active area of the fabricated photoanode. A comparative concentration of the amount of dye loaded for the various combinations of photoanode is tabulated in Table 6.4. The amount of the dye loaded was calculated by measuring the dye de-loaded/desorbed from the photoanode using UV-vis spectra (Figure 6.7c).

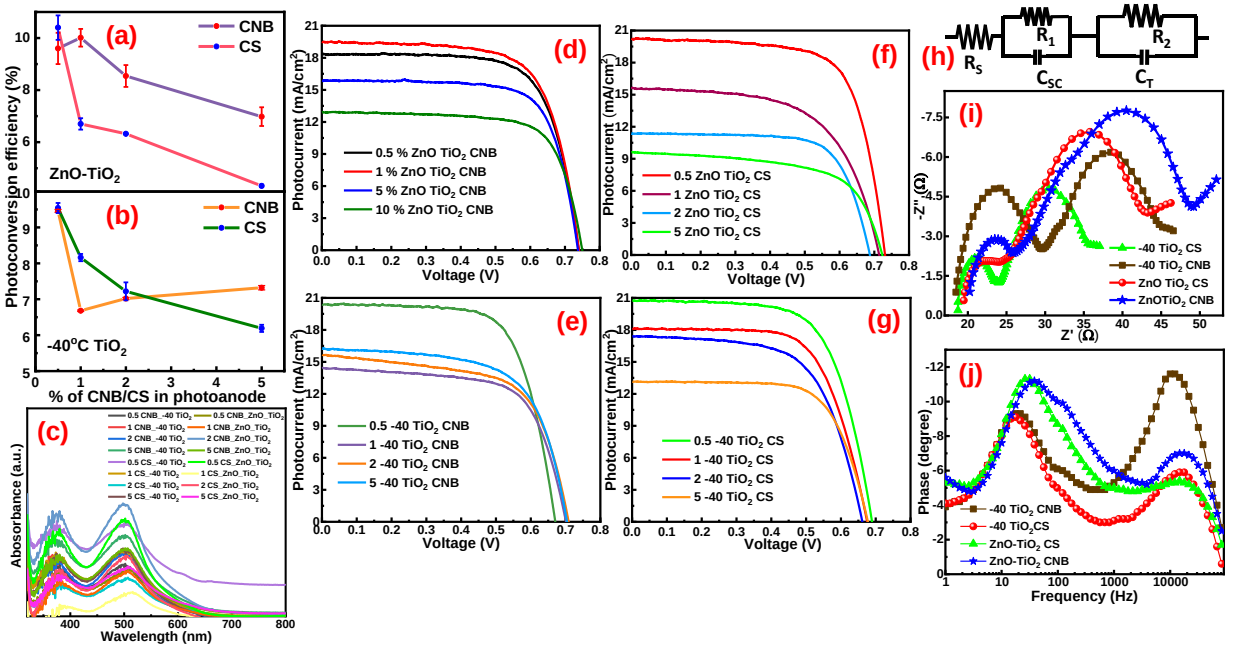

Figure 6.7: (a, b) Plot summing up the PCE of increasing loading % of CNB and CS based photoanodes with our earlier reported material (Shejale, Laishram et al. 2016, Shejale, Laishram et al. 2017) (c) UV measurement of dye loading of different photoanodes for DSSC (d, f) Device parameters of fabricated DSSCs using the synthesized nanomaterials (dye N719, 0.5 mM and active area 0.04 cm^2) – IV graphs of the synthesized CNB and CS in combination with different % ZnO doped TiO_2 and TiO_2 synthesized at -40 °C (e and g), Nyquist plot (i) and bode plot (j) of the best performing solar cell, (h) equivalent model circuit used in fitting.

Table 6.3. Photovoltaic DSSC data obtained from I-V and EIS

Sample Name	V_{OC} *(V)*	J_{SC} *(mA/cm²)*	*PCE, η (%)*	*FF (%)*	R_S *(Ω)*	R_1 *(Ω)*	R_2 *(Ω)*	C_{SC}	C_T	τ *(ms)*
0.5% CNB + ZnO-TiO_2	0.75	19.47	9.6	65.56	20.62	10.61	0.11	2.50 x10^{-4}	2.27 x10^{-6}	26
0.5% CS + ZnO-TiO_2	0.73	20.20	10.40	70.14	22.96	12.97	4.81	2.58 x10^{-4}	4.52 x10^{-6}	32
0.5% CNB + -40_TiO_2	0.67	20.37	9.46	68.59	22.96	15.08	10.44	5.35 x10^{-4}	2.47 x10^{-6}	46
0.5% CS + -40_TiO_2	0.70	20.75	9.54	66.05	18.77	8.97	5.06	8.64 x10^{-4}	3.35 x10^{-6}	56

It was observed that DSSC fabricated using the 0.5% CS_ZnO_TiO_2 photoanode showing the highest efficiency of 10.40 % among all the other combinations of photoanodes displayed maximum concentration (3.25x10^{-10} M/cm^2) of dye adsorption as can be seen from Table 6.4. In addition to this, the EIS study was done to investigate the electron transport properties of the system and its subsequent fitting of the Nyquist plots (Figure 6.7i) is given in Table 6.3. Here, R_S is the series resistance, R_1 and R_2 represent the counter electrode and electrolyte charge transfer resistance respectively and C_{SC} and C_T represent the chemical capacitance and the Pt- electrolyte capacitance. τ represents the recombination lifetimes of the electrons involved in the process and is calculated from the Bode plot in Figure 6.7j. The equivalent circuit model best fitted to the Nyquist plot is given in Figure 6.7h. It is observed that the charge transfer resistance in the TiO_2/Dye/Electrolyte interface is greatly reduced for 0.5 %

CS and ZnO-TiO_2 composite photoanode. It is observed that the charge transfer resistance between the TiO_2/dye/electrolyte interface and the charge transport resistance at the Pt counter electrode is decrease for the 0.5% CS + ZnO/TiO_2. This along with good conductivity of the carbon increases the electron transport in the fabricated device enhancing the overall photoconversion efficiency (PCE). Moreover, the concoction of high surface area carbon nanomaterials and different forms of TiO_2 formulate good point contact and uniform homogeneous compact layer between the photoanode and FTO glass substrate, providing an overall increase in PCE.

Table 6.4. Result of dye de-loading measured with UV-vis spectrometer where, ε is the coefficient of absorbance with 1.4 X 10^4 for N_3 dye, l is the length of the cuvette (1 cm)

Sl. No	*Sample*	*Absorbance (A)*	*Concentration of dye* $c = A/l\varepsilon (M/cm^2)$
1.	0.5 CNB_-40 TiO_2	0.0498	3.43×10^{-10}
2.	1 CNB_-40 TiO_2	0.0604	4.17×10^{-10}
3.	2 CNB_-40 TiO_2	0.0601	4.14×10^{-10}
4.	5 CNB_-40 TiO_2	0.0783	5.4×10^{-10}
5.	0.5 CS_-40 TiO_2	0.0882	6.08×10^{-10}
6.	1 CS_-40 TiO_2	0.0627	4.32×10^{-10}
7.	2 CS_-40 TiO_2	0.0362	2.50×10^{-10}
8.	5 CS_-40 TiO_2	0.0637	4.39×10^{-10}
9.	0.5 CNB_ZnO_TiO_2	0.0446	3.08×10^{-10}
10.	1 CNB_ZnO_TiO_2	0.0435	3.0×10^{-10}
11.	2 CNB_ZnO_TiO_2	0.108	7.45×10^{-10}
12.	5 CNB_ZnO_TiO_2	0.0644	4.44×10^{-10}
13.	0.5 CS_ZnO_TiO_2	0.0918	6.33×10^{-10}
14.	1 CS_ZnO_TiO_2	0.0228	1.57×10^{-10}
15.	2 CS_ZnO_TiO_2	0.0564	3.89×10^{-10}
16.	5 CS_ZnO_TiO_2	0.0471	3.25×10^{-10}

6.2.6. Application as counter electrode for DSSC

Furthermore, the prepared CNB and CS were used as a counter electrode in DSSC with the highest performing 0.5% ZnO/TiO_2 as the photoanode, the preparation method is given in the experimental section. The exchange and limiting current density, J_0 and J_{lim} are defined by the sharp slope and the horizontal trend in the Tafel curve as shown in Figure 6.8a. It can be observed that the slope is highest for CNB indicating the highest J_0 in the CNB material and is in accordance with that of the EIS data showing the smallest R_{ct} for CNB. Comparable result were observed for the Pt and CS samples. To further realize the efficiency as catalytic materials for the counter electrode in DSSC, electrochemical properties measurements such as CV and electrochemical impedance measurements were performed (see Figure 6.8b and c). The prepared carbon samples, along with N dopant and good porosity gave huge advantage for efficient diffusion of the ions for a proper electrocatalytic reaction.(Wang, Gao et al. 2015) In this study both CNB and CS were subjected to catalytic I_3^- reduction and compared with the Pt counterpart. It can be seen from Figure 6.8b that the current density is superior for both the carbon nanospheres with CS showing highest followed by CNB and Pt. However, Pt shows prominent peaks, unlike the carbon counter parts is an indication of the presence of capacitive current. It can also be inferred that there are two prominent oxidation and reduction peaks with the peak to peak ratio, E_{PP} (potential difference between cathodic and anodic peak) calculated in order as CNB < CS < Pt.

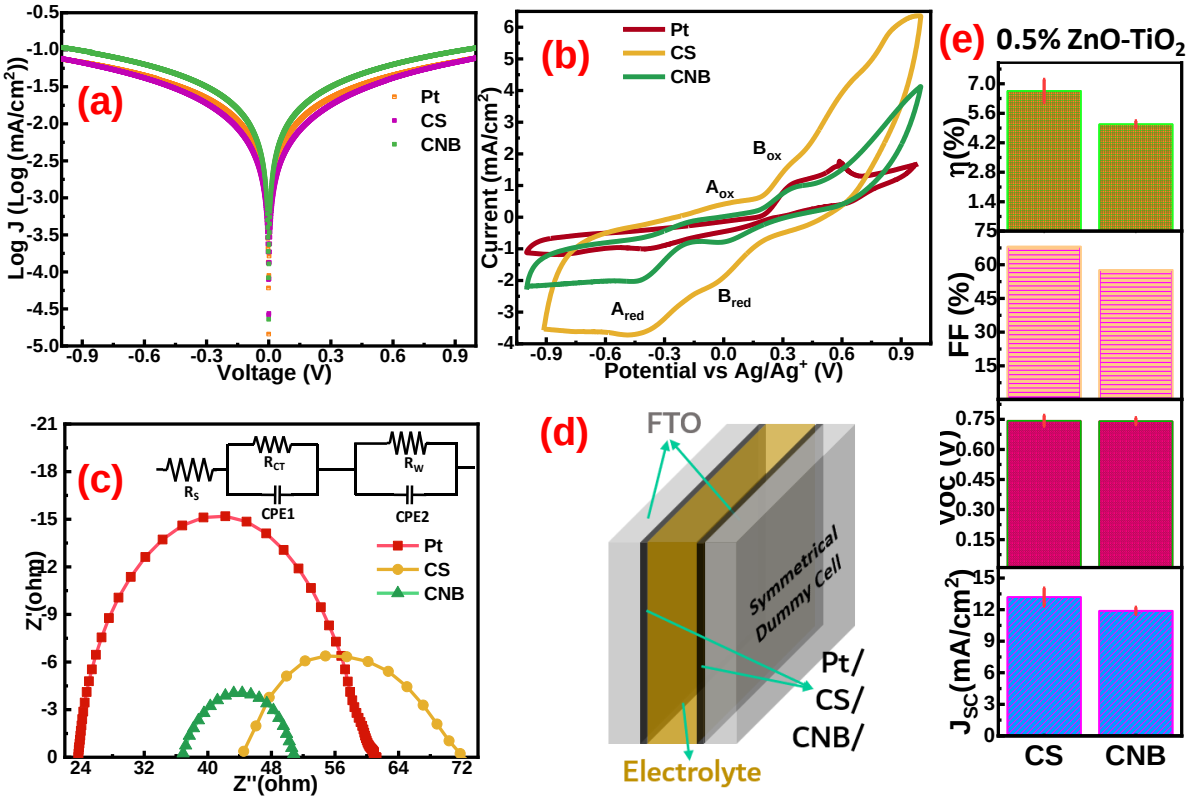

Figure 6.8: (a) Tafel plot, (b) cyclic voltammetry curves at 20 mV/s scan rate, (c) Nyquist plot with its equivalent circuit diagram (inset) of dummy cell (Consists of FTO coated Pt/CS/CNB sandwitched together and filled with 150 mM electrolyte where active area was 0.25 cm^2). R_s: series resistance, R_{ct}, R_w: charge transfer resistance, CPE: constant phase element, (d) schematic of a symmetrical dummy cell and (e) bar graph showing the IV data constructed using the synthesized carbon nanomaterials.

The oxidation and the reduction peaks correspond to the redox activity of the electrolyte as I_2 to I_3^- and I_3^- to I^-.(Krishnapriya, Praneetha et al. 2017) The reduced E_{PP} and high current density in the carbon materials suggests the improved activity for catalytically reducing I_3^- to I^- and improved capacitive behaviour attributing to high current density. This is due to the combined effect of the high specific surface area accompanied by good porosity of the synthesized materials and also due to conceivable improvement in the thickness of the prepared counter electrodes. An illustrative bar graph representation summarizing the observed J_{SC}, V_{OC}, FF and PCE (η) of the fabricated DSSC devices with CNB and CS as a counter electrode with 0.5 % $ZnO\text{-}TiO_2$ is shown in Figure 6.8e. Although, similar V_{OC} was observed for both the material, higher FF and J_{SC} were observed which led to an increase in efficiency for CS based devices. The electrochemical impedance study was carried out to understand the effect of charge transport. The Nyquist plot in Figure 6.8c shows the charge transport and transfer activities in the symmetrical dummy cell (schematic in Figure 6.8d). The Nyquist plot is fitted according to the equivalent circuit diagram given in the inset of Figure 6.8c. The calculated charge transfer resistance, R_{ct} was found to be 7 Ω cm^{-2}, 57 Ω cm^{-2} and 30 Ω cm^{-2} respectively for CNB, CS and Pt. The lower R_{ct} could be attributed to the faster charge transfer process due to catalytically active large active electrode area.

6.2.7. Application as material for supercapacitor

The synthesized CS and CNB were analysed as potential materials for its energy storage properties by electrochemical characterizations such as cyclic voltammetry (CV), impedance and Tafel studies. All the electrochemical studies were performed using three-electrode configurations in 0.1 mM Na_2SO_4 aqueous electrolyte. Figure 6.9a, c and d shows the CV curve obtained from CS and CNB at 100 mV/s and at various scan rates. It was observed that both CS and CNB exhibited near rectangular-shaped curves without any prominent redox potential peaks, indicating a double-layer capacitive behaviour, good electrochemical reversibility and high-power characteristics. The current density and area under the CV curve for CS are

apparently much higher than the CNB at the 100mV/s scan rate which leads to high specific capacitance (577 F/g) compared to CNB (458 F/g).

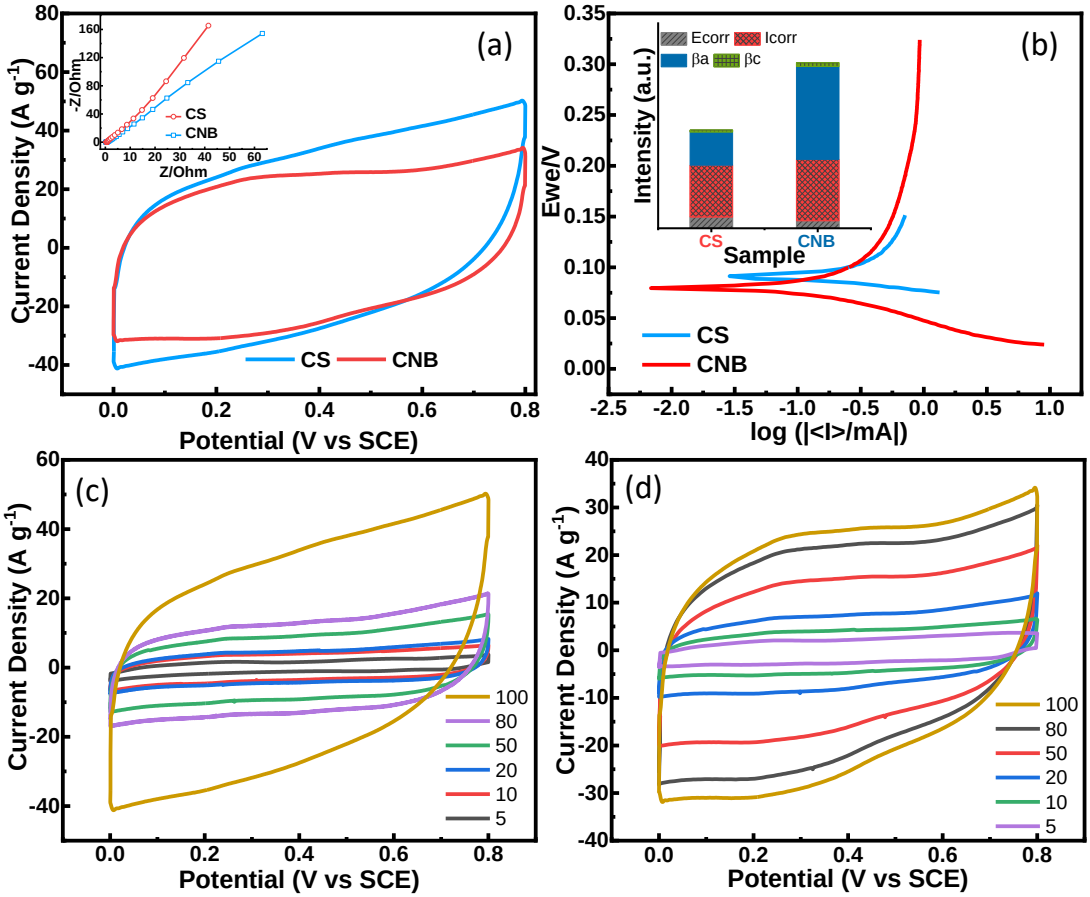

Figure 6.9: (a) Cyclic voltammetry plots (0.1mM Na_2SO_4, applied voltage 0-0.8V and scan rate 100 mV/s) with inset plot shows Nyquist plot and (b) Tafel curves with inset bar graph summarizing Tafel parameters and other electrokinetic parameters (E_{corr} corrosion potential (mV), I_{corr} corrosion current (μA), β_a anodic and β_c cathodic β Tafel constant (mV) of CS and CNB, CV obtained from CS (c) and CNB (d) at various scan rates.

This is due to the faradaic pseudo capacitors exhibiting much higher specific capacitance with reversible multielectron redox faradaic reactions. Inset of Figure 6.9a is the Nyquist plots of CS and CNB electrodes in the frequency range from 10Hz to 10KHz. The impedance spectra show semicircles in the high frequency, an anamorphic semicircle in the medium frequency and straight lines nearly vertical to the real axis in the low-frequency range. The ideal capacitor always exhibits a vertical line at low frequency.(Wang, Gao et al. 2015) The presence of semicircles of supercapacitors is attributed to the faradic reaction that occurred at the electrode surface. At high frequency, CS electrode has much smaller charge-transfer resistance (almost straight line), suggesting the fast charge transfer and less recombination. However, semi-circular plots at low frequencies were observed for the electrode with CNB, a resultant of the slow ion diffusion behaviour. Additionally, the improved specific capacitance for CS is attributed to its high specific surface area and e^- transport path, highly conducting C in a solid sphere with high effective surface area increases its contact with the electrolyte. The utilization and pseudo capacitance of active materials are significantly improved. The Tafel plot is used to quantify the polarization results and it gives corrosion rate directly and Tafel plots of CS and CNB are shown in Figure 6.9b and Tafel parameters and other electro kinetic parameters are summarized in the inset of Figure 6.9b. The anodic polarization profiles inferred the material dissolution behaviour in aggressive media. All the measurement was performed out in Na_2SO_4 solution at open circuit potential of respective electrodes. The corrosion potential value of electrode was shifted more positive with a corresponding hollow morphology, such results suggest that from both surfaces from inner and outer were responsible for these values.

6.3 Conclusion

In summary, highly homogenous nitrogen-enriched carbon spheres as well as carbon nanobubbles were successfully synthesized by a modified Stöber reaction route and a comparative study on the performance of these materials as electrode materials for DSSCs, supercapacitors and CO_2 adsorption. Additionally, a systematic study on the integration of highly efficient TiO_2 and ZnO as composite photoanode material were performed. When CS and CNB materials were applied as DSSC photoanode material with TiO_2/ZnO heterostructures, the fabricated devices showed improved PV performance with remarkable efficiency of 10.40%, excellent point contact and conductivity. The improved current density, open circuit potential and the overall efficiency were found to be due to reduced charge recombination, increment in the charge collection and improvement in the transport of charge carriers through composite photoanode. The mesoporous structure of CS material offered much large surface area for effective capture of CO_2 even at low pressure. Electrochemical studies of CNB and CS showed reduced E_{PP} and high current density; suggested the improved catalytic activity for reducing I_3^- to I^- and good capacitive behaviour due to high current density. Both CS and CNB exhibited near rectangular-shaped CV curves without any prominent redox potential peaks that indicated the double-layer capacitive behaviour, good electrochemical reversibility and high-power characteristics essential for the supercapacitor application. We successfully established our proposition with various characterization techniques and applications that solid CS with larger size and higher surface area yield better output in CO_2 capture, photo conversion efficiency and as potential material for supercapacitor application. The current investigation is anticipated to open up new possibilities for the design and fabrication of homogenous multifunctional carbon nanostructures for application in various energy conversion and storage devices.

...